VALIDATION OF HELIOSEISMOLOGY THROUGH FORWARD MODELING: REALIZATION NOISE SUBTRACTION AND KERNELS

S. M. HANASOGE,[1,2] T. L. DUVALL, JR.,[3] AND S. COUVIDAT[1]

ABSTRACT

Through a series of numerical simulations of the near-surface acoustic wavefield of the Sun, we show the utility of the forward approach in local helioseismology. We demonstrate and apply a method to *subtract* a large fraction of the realization noise from the simulated data. The ability to attain high signal-to-noise ratios from brief forward calculations implies that computational resources are less of a bottleneck, making this alternate method for investigations of the solar interior very feasible. We put this method to use by deriving sensitivity kernels for sound-speed perturbations and source suppression for the background state in our computations using techniques of time-distance helioseismology, all from merely 48 hr of artificial data.

Subject headings: hydrodynamics — Sun: helioseismology — Sun: interior — Sun: oscillations — waves

1. INTRODUCTION

For almost two decades, methods of local helioseismology (e.g., Hill 1988; Braun et al. 1987) have been applied to infer properties of the solar interior, with varied degrees of success (for a comprehensive review, see Gizon & Birch 2005). The predominant approach is to construct and subsequently invert models that relate observations to interior properties. As observations have become increasingly sophisticated, the need for refined forward modeling has become apparent. One reason the forward approach is crucial is that although the resonant mechanical modes of the Sun (the diagnostic agents of helioseismology) have been studied carefully, there are still many unmodeled curious wave properties that may prove significant. For example, finite wavelength effects cast doubt on the validity of the ray approximation in some situations (e.g., Hung et al. 2001; Couvidat et al. 2004); magnetic fields in the case of sunspots are potentially nontrivial contributors to the wavefield. Although these implications have been known for a while now, a systematic means of investigating such factors has only recently been constructed. Such studies are difficult to conduct by purely analytical means, requiring the introduction of numerical methods to solve the constituent governing equations of wave motion (e.g., Tong et al. 2003; Hanasoge et al. 2006; Parchevsky & Kosovichev 2006; Shelyag et al. 2006).

The effects of sound-speed perturbations on acoustic waves have been investigated in the past (e.g., Jensen et al. 2003; Jensen & Pijpers 2003; Birch et al. 2004). In fact, Jensen et al. (2003) constructed a forward model to compute the wavefield associated with a sunspot-type sound-speed profile containing a near-surface decrease in the sound speed and an increase in the deeper layers.

Sensitivity kernels are mathematical structures that relate shifts in observational metrics such as travel times, resonant frequencies, etc., to the anomalies that cause them. Birch & Kosovichev (2000) and Gizon & Birch (2002) introduced finite frequency sensitivity kernels for helioseismology (note: we will use the terms "finite wavelength" and "finite frequency" interchangeably in future discussions) that include wave effects in the Born limit, to invert for interior sound speed, damping, and source perturbations. The computation of these kernels is a nontrivial affair. Moreover, these kernels are obtained in the single-scattering limit, and the Born approximation itself may not be applicable for problems such as inversions of sunspots (A. C. Birch 2007, private communication). In this paper, we measure kernels at the photospheric level from simulations in two cases for which the Born limit is valid and published kernels are available for comparison (Gizon & Birch 2002; Birch et al. 2004).

We also introduce the idea of noise subtraction, on the basis of which we can obtain large signal-to-noise ratio (SNR) improvement in our simulations. When applying this concept, for certain problems, with as little as 40 hr of computing time, the signal can be boosted by so much that the eventual SNR is at the same level as that of 2 yr of solar data. In § 2 we discuss the numerical procedure applied to compute the wavefield. The idea of noise subtraction is introduced in § 3, along with results that demonstrate its effectiveness. Travel times for the simulated wavefield are estimated with the technique of surface focusing in § 4. We show how noise subtraction affects the travel times and also validate the results from the simulations in this section. An alternative method to compute kernels for helioseismology is shown to be effective in § 5. We summarize our results and draw conclusions in § 6.

2. THE SIMULATION

The acoustic wavefield is simulated by numerically solving the linearized three-dimensional (3D) Euler equations in Cartesian geometry:

$$\partial_t \rho = -\nabla \cdot (\rho_0 \boldsymbol{v}) - \Gamma \rho, \tag{1}$$

$$\partial_t \boldsymbol{v} = -\frac{1}{\rho_0} \nabla p - \frac{\rho}{\rho_0} g \hat{\boldsymbol{e}}_z + \boldsymbol{S} - \Gamma \boldsymbol{v}, \tag{2}$$

$$\partial_t p = \boldsymbol{v} \cdot \nabla p_0 - \rho_0 c^2 \nabla \cdot \boldsymbol{v} - \Gamma p, \tag{3}$$

where ρ and ρ_0 are the fluctuating and time-stationary background density, respectively; p and p_0 are the fluctuating and time-stationary background pressure, respectively; $\boldsymbol{v}$ is the fluctuating

[1] W. W. Hansen Experimental Physics Laboratory, Stanford University, Stanford, CA 94305; shravan@stanford.edu.

[2] Department of Mechanical Engineering, Stanford University, Stanford, CA 94305.

[3] Solar Physics Laboratory, NASA Goddard Space Flight Center, Greenbelt, MD 20771.
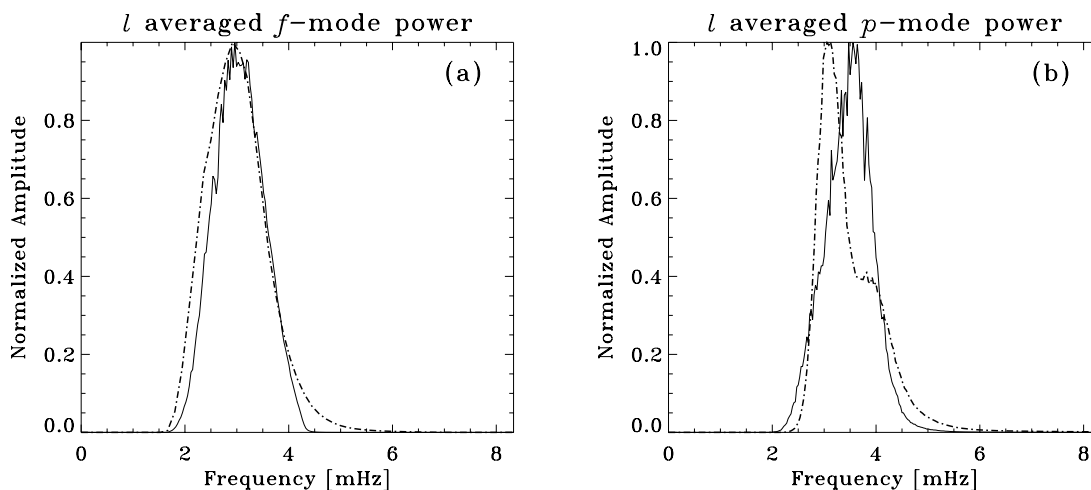
FIG. 1.—Comparison of wavenumber-averaged power profiles of MDI high-resolution data (*dot-dashed lines*) and simulations (*solid lines*) as a function of frequency. The *f*-mode power distribution in (*a*) is quite representative of the observations. Because of the lack of damping, the *p*-mode power distribution in (*b*) does not do quite so well. A phase-speed filter (filter B of Birch et al. 2004) was applied to obtain (*b*).

vector velocity; $g = g(z)$ is gravity with direction vector $-\hat{\boldsymbol{e}}_z$; $c = c(x, y, z)$ is the sound speed; $\Gamma = \Gamma(x, y, z) > 0$ is a damping sponge that enhances wave absorption at the boundaries; and $\boldsymbol{S}$ is the source term. We employ a Cartesian coordinate system (x, y, z), with $\hat{\boldsymbol{e}}_z$ denoting the unit vector along the vertical or z-axis and t denoting time. In sequential order, equations (1)–(3) enforce mass, momentum, and energy conservation, respectively. In interior regions of the computational box (away from the boundaries), solutions to the above equations are adiabatic, since equation (3) is applicable only in the case of adiabatic oscillations (e.g., Hanasoge et al. 2006) and there are no other damping terms.

In our computations, waves are excited by a vertically directed dipolar source function, $\boldsymbol{S} = S(x, y, z, t)\hat{\boldsymbol{e}}_z$, similar to the function described in Hanasoge et al. (2006). The function $S(x, y, z, t)$ is highly localized along the z-axis, described by a Gaussian with a FWHM of 200 km. Adopting the approach described in Hanasoge et al. (2006), we start our analysis in the frequency-horizontal wavenumber Fourier space. Because scattering processes are sensitive to the frequency and wavelengths of interacting waves, we attempt to mimic the solar acoustic power spectral distribution as closely as possible (see Fig. 1). As for the dependence of the excitation function on horizontal wavenumbers, each coefficient in Fourier space is assigned a value from the output of a Gaussian-distributed zero-mean random number generator (the Ziggurat algorithm, available online from NETLIB). This results in uniform power across wavenumbers, which is somewhat different in the Sun because the sources are at granular scales and there is some dependence of power on wavenumber. To achieve the demands placed on the frequency dependence of the spectrum, we multiply these coefficients by an a priori specified frequency envelope. Lastly, we prescribe the excitation function so that it possesses no power beyond (to the right of) the *f*-mode ridge, where modal power in the Sun is practically nonexistent anyway. The inverse Fourier transform of this function provides us with a spatiotemporal description of the multiple-source exciter, $S(x, y, z, t)$.

In the Sun, the competing effects of damping, which has a superlinear frequency dependence, and mode mass, which decreases with frequency, create a power maximum at $\nu = 3$ mHz. However, one immediately realizes that solar damping rates are by no means simple functions of frequency, with the consequence that fully including these dissipation rates in our time domain calculations is made all but impossible. Moreover, the aim of these calculations is to deconstruct the influences of perturbative forces, one of which undoubtedly is damping (e.g., Gizon & Birch 2002). Therefore, although approximate representations of the solar damping function could be incorporated into the equations above, we make the active choice to leave them out at present, with the full intention of pursuing a greater understanding of the effects of dissipation at a future occasion.

Revisiting the background state, we use the time-stationary properties p_0, ρ_0, g, and c given by the convectively stable model of Hanasoge et al. (2006), based on model S (Christensen-Dalsgaard et al. 1996). Without additional artificial stabilization, simulations of wave activity in the near-surface layers tend to blow up very rapidly due to exponentially growing linear convective instabilities. This stabilization results in a modified dispersion relation for *p*-modes, not quite the same as it is for the Sun, but mercifully, close enough that existing methods of helioseismology may be applied with few alterations. The functional dependence of c presented in the model of Hanasoge et al. (2006) is entirely radial (vertical); for experiments with sound-speed perturbations, we alter c so that it becomes a 3D function of space while keeping p_0 and ρ_0 constant. The latter variables are kept constant so that the delicate hydrostatic balance remains undisturbed, which, if tampered with, results in a Kelvin-Helmholtz instability. As seen in equation (4), this means that when we alter the sound speed and not the pressure or density, the first adiabatic index Γ_1 changes in the same sense, since

$$c = \sqrt{\frac{\Gamma_1 p_0}{\rho_0}}. \tag{4}$$

It can be shown that the degree of convective instability, characterized by the Brünt-Väisälä frequency N ($N^2 < 0$ indicates instability) in equation (5), increases when Γ_1 (or c) is reduced:

$$N^2 = g\left(\frac{1}{\Gamma_1}\frac{\partial \ln p_0}{\partial z} - \frac{\partial \ln \rho_0}{\partial z}\right). \tag{5}$$

Consequently, all our theoretical experiments are with local increases in sound speed. Our expectation is that decreases in sound speed affect helioseismic metrics in the opposite sense as corresponding increases would.
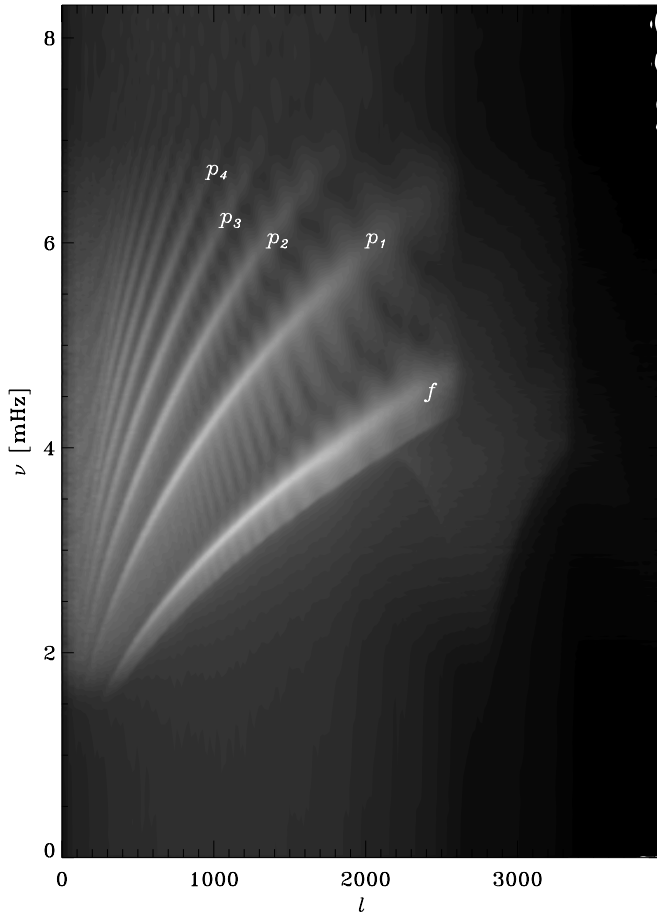
Fig. 2.—"Quiet" power spectrum obtained from a simulation in a $200 \times 200 \times 30$ Mm³ box. The horizontal axis is the spherical harmonic degree, l, and the vertical axis is the frequency, in units of mHz.
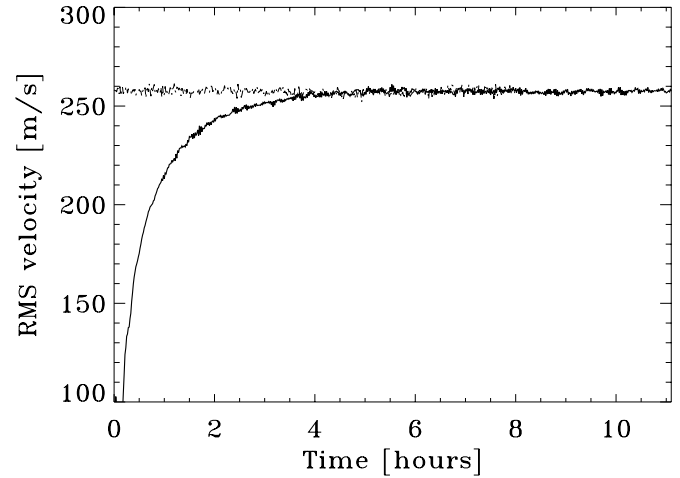

Fig. 3.—Spatial rms velocity at the photosphere of a simulation (*thick line*) as compared to MDI high-resolution data (*thin line*) as a function of time. The system appears to achieve statistical stationarity 4.5 hr into the simulation. Because the system is linear, we can scale velocities by an arbitrary factor as long as they are much smaller than the local sound speed; in this case, velocities have been scaled so as to allow comparison with solar values.

2.1. *Numerical Algorithm*

The computational domain is a cuboid that straddles the solar surface, extending from approximately 30 Mm below the photosphere to 2 Mm into the atmosphere. The vertical (radial) grid spacing is such that acoustic travel time between adjacent grid points is constant, while the horizontal grid points are equally spaced. The damping sponge described in the previous section (§ 2) is placed adjacent to the six boundaries of the computational box. It is important that the function describing the damping layer decays sufficiently smoothly away from the boundary so that no wave reflections occur at the interface of the absorbent region. Absorbing boundary conditions (Thompson 1990) are enforced at all boundaries. We choose absorbing over periodic boundaries because we want to avoid the issue of dealing with periodicities associated with the presence of a perturbation.

Derivatives are calculated using sixth-order compact finite differences (Lele 1992). The solution is evolved in time using an optimized five-stage second-order Runge-Kutta scheme (Hu et al. 1996). To avoid aliasing, we apply the two-thirds rule (Orszag 1970), requiring that the maximum captured wavenumber be at most two-thirds the number of grid points. In order to avoid vertical (radial) aliasing and the subsequent spectral blocking, we apply the dealiasing procedure described in Hanasoge & Duvall (2007) once every minute in solar time. We also dealias variables in the horizontal directions by applying a smooth filter that diminishes the upper third of the spectrum and leaves the important lower two-thirds untouched (also at the

rate of once per minute). All fast Fourier transforms (FFTs) are performed using the freely distributed set of routines, the FFTW.

In order to achieve a comparable computation–to–wall clock time ratio, the code was parallelized according to the Message Passing Interface (MPI) Standard. The domain distribution algorithm is similar to the method described in Hanasoge & Duvall (2006). The computational box is distributed along the *y*-axis; all points on the *x*- and *z*-axes for a given point on the *y*-axis are located in-processor. The data are transposed and redistributed between processors when the solution has to be filtered and when derivatives along the *y*-axis need to be computed. It is probably true that greater parallel efficiencies may be achieved if the domain distribution is along all axes. However, incumbent to determining the optimal parallel configuration is the investment of considerable time, no doubt entailing many tedious hours of programming and debugging. At present, we only treat relatively small problems ($200 \times 200 \times 40$ Mm³ is the biggest box) and achieve ratios of 1 : 1 (usually better) computing to real time. Seeing little merit in further code optimization, we have relegated such investigations to the future.

2.2. *Power Spectrum*

The modal distribution of power that we recover upon putting together all the ideas discussed above and subsequently performing the computation is shown in Figure 2. We do not have a convincing explanation for the oddly shaped interridge mode tails. Beyond the demarcation of the excitation profile, seen just below the *f*-mode ridge, excitation levels drop to zero. Also, in accordance with the two-thirds rule, the excitation is Fourier-limited, not extending beyond two-thirds of the spatial Nyquist wavenumber. The rms spatially averaged velocity as a function of time is shown in Figure 3; the simulation in this case is seen to achieve statistical stationarity in 4.5 hr. This timescale corresponds to at least a few bounces of the largest wavelength acoustic waves, and presumably full stationarity is reached when the balance between the forcing and the absorbent layers (at all boundaries) is struck.

3. NOISE SUBTRACTION

Given that we have full control over the excitation mechanism and source function, we can achieve a high SNR in the artificial
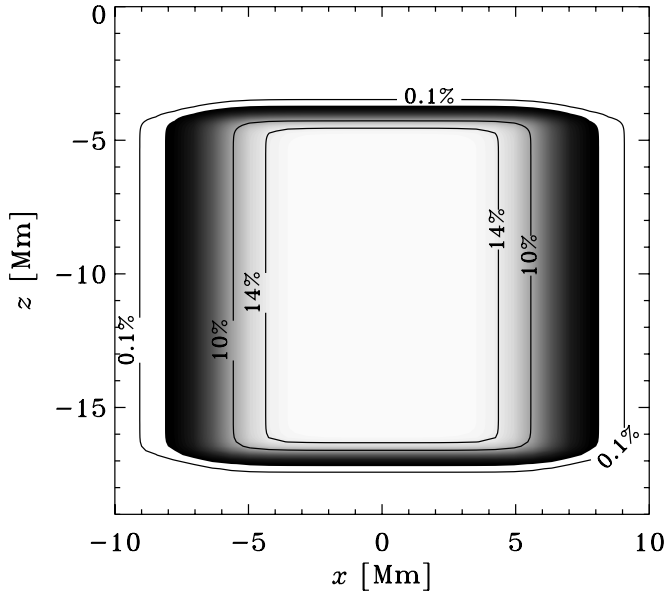
Fig. 4.—Vertical cut in the sound-speed perturbation discussed in Fig. 5. The labels on the isocontours show the amplitude of $\delta c^2/c^2$. The perturbation is cylindrically symmetric about the $x = 0$ line.

data by *subtracting* the noise out (Werne et al. 2004). In other words, having computed a source function, we perform two simulations, one with no perturbations (the "quiet" simulation) and another with the perturbation of interest (shown in Fig. 4). Evidence of the ability of this method is demonstrated by displaying the time-averaged rms of the velocity differences between a quiet and perturbed model in Figure 5b. Compare this to Figure 5a, which is the time-averaged rms velocity of the perturbed model. Subsequently, we can subtract the travel times of the quiet simulation data from those of its perturbed cousin, and, depending on the size of the perturbation in comparison to the wavelength, excellent SNR properties can be achieved. The instantaneous difference is shown in Figure 5c. In some cases in which the perturbation is highly subwavelength in size, the SNR after noise subtraction is as much as 1000:1. In subsequent sections, we will elaborate further on the applications of this technique.

4. TRAVEL TIMES WITH SURFACE FOCUSING

The time-distance helioseismic formalism introduced by Duvall et al. (1993) is based on the computation of cross-covariances between solar oscillation signals at two locations r_1 and r_2 on the solar surface ($z = 0$). Due to the stochastic excitation of acoustic waves (by convective motions in the Sun) and to the superposition of a large number of waves of different horizontal phase velocities $v_{ph} = \omega/k$, where k is the horizontal wavenumber and ω is the temporal angular frequency, the cross-covariances are very noisy and need to be phase-speed filtered and averaged (Duvall et al. 1997). The Doppler velocity datacube $\phi(r, t)$ is phase-speed filtered in the Fourier domain using a Gaussian filter $F(k, \omega; \Delta)$ for each travel distance $\Delta = |r_2 - r_1|$:

$$F(k, \omega; \Delta) = \exp\left[-\frac{(\omega/k - v)^2}{2\delta v^2}\right], \qquad (6)$$

where the central phase speed v is derived from the solar model describing the oscillation power spectrum. For p-modes in the ray approximation, v corresponds to ω/k at the lower turning point of a ray that traverses a horizontal distance Δ between successive reflections. The filter width δv is chosen empirically.
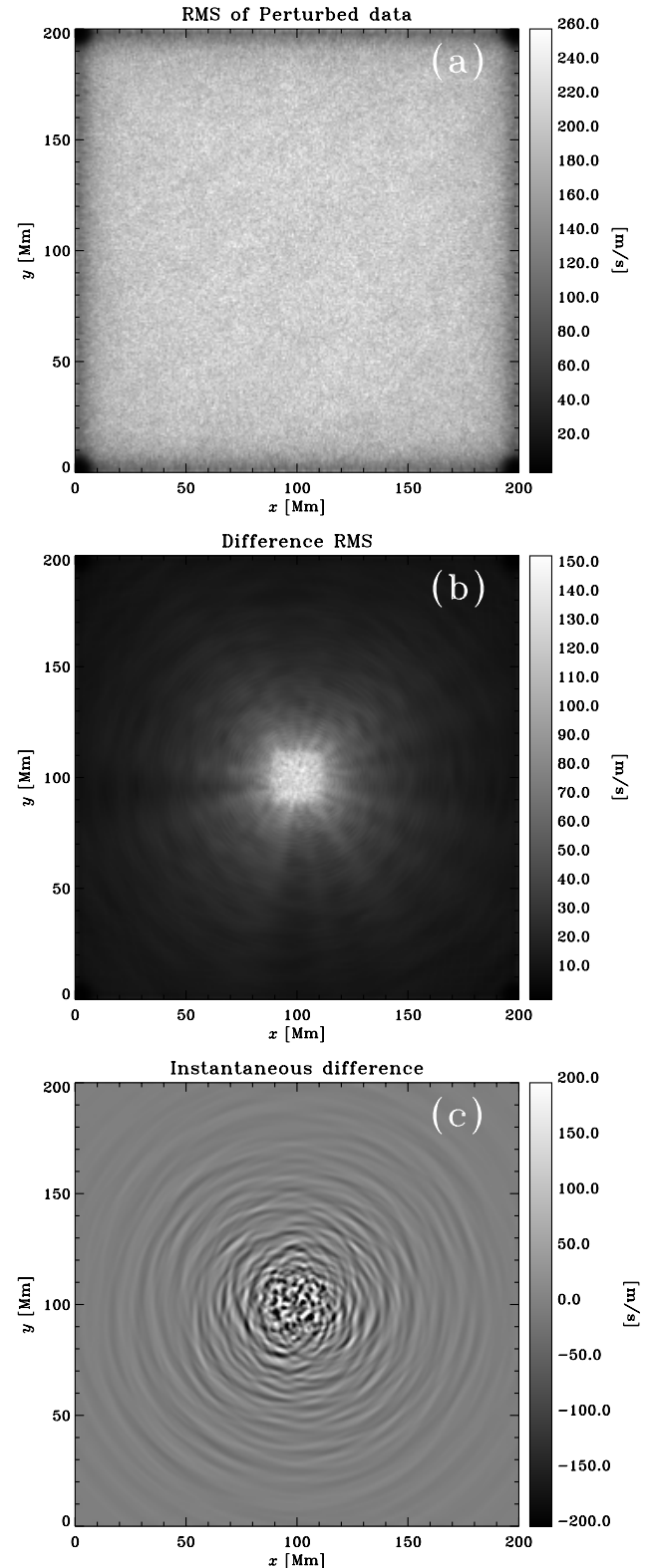

Fig. 5.—(a) Time-averaged rms velocity of the wavefield interacting with a 12 Mm sized sound-speed increase (shown in Fig. 4), centered around $(x, y, z) = (100\text{ Mm}, 100\text{ Mm}, -10\text{ Mm})$. The sound-speed anomaly is entirely invisible in (a). The darkening toward the spatial edges of the frame is due to the absorbent sponge at work. (b) Time-averaged rms velocity difference of the perturbed datacube and its quiet counterpart. The difference between the quiet and perturbed datacubes is greatest at the location of the perturbation due to enhanced scattering. (c) Instantaneous difference between the perturbed and related quiet data 100 (solar) minutes into the simulation. The anomaly is a scatterer, creating ripples in the wavefield just like a pebble dropped onto the surface of still water. Fine wave structure is visible at the location of the perturbation.
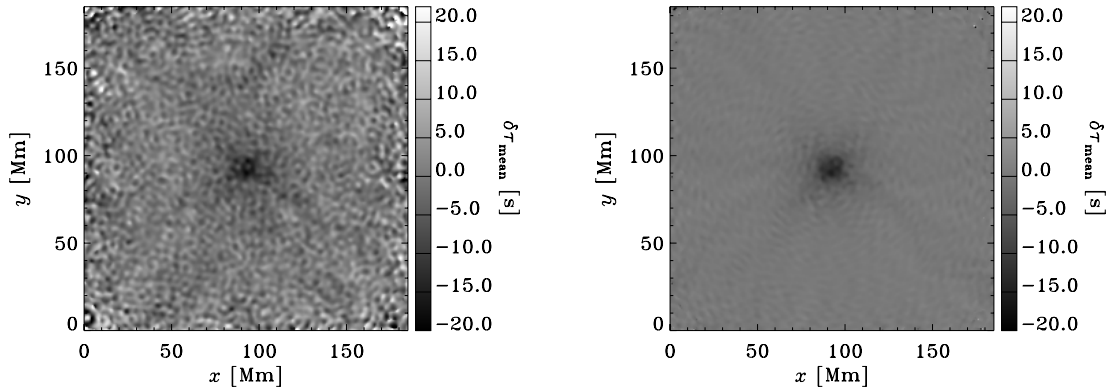
Fig. 6.—Example of a mean travel-time perturbation map $\delta\tau_{mean}(\mathbf{r}, \Delta)$ for $\Delta = 30.55$ Mm. *Left*: Before the quiet map subtraction. *Right*: After the subtraction.

The standard method is then to average point-to-point cross-covariances over an annulus centered on $\mathbf{r}_1$ and with a radius Δ. Such point-to-annulus cross-covariances are computed for several distances Δ (55 in this paper) and then averaged by groups of five distances to further increase their SNR. A detailed explanation of all the steps in the analysis process can be found in, e.g., Couvidat et al. (2006). Table 1 in Appendix A lists the distances Δ and phase-speed filter characteristics used here. These values are slightly different from the solar case because of the modified description of the background model.

The point-to-annulus cross-covariances are fitted by two Gabor wavelets (Kosovichev & Duvall 1997), one each for the positive and negative times. To select the first-bounce ridge, we multiply the temporal cross-covariances by 14 minute wide rectangular window functions prior to the fit. The center time t_0 of these windows is listed in Table 1. The fitting procedure returns the ingoing (subscript i) and outgoing (subscript o) phase travel times $\tau_{i/o}(\mathbf{r}, \Delta)$. The average of these two travel times, $\tau_{mean}(\mathbf{r}, \Delta)$, is at first approximation sensitive only to the sound speed $c(\mathbf{r})$ in the region traversed by the wavepacket (see eq. [7]), and similarly the difference $\tau_{diff}(\mathbf{r}, \Delta)$ is sensitive only to material flows. Note that by wavepacket, we mean a collection of waves of different frequencies and wavelengths that satisfy a specific dispersion relation, $\omega = \omega(k)$.

4.1. Results

We separately compute the acoustic wavefield in the presence of a sound-speed anomaly and the unperturbed counterpart with the same forcing func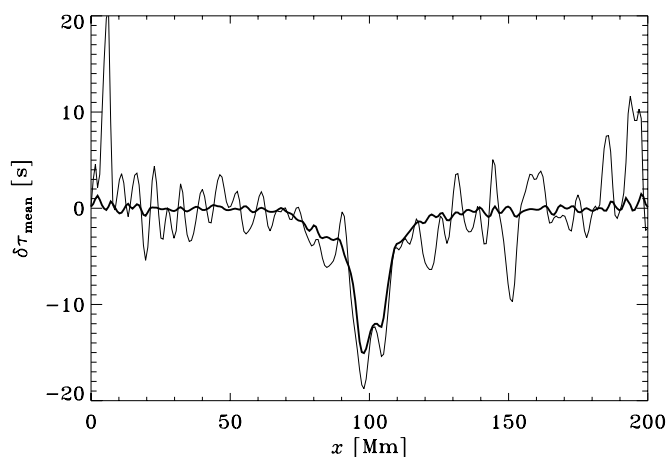tion. Subsequently, we derive travel-time maps related to these datacubes by applying the method described in § 4. Here we focus on results related to a cylindrical sound-speed perturbation (see Fig. 4) with a horizontal radius of about 6 Mm, a height of 12 Mm, centered at a depth of 10 Mm, and with a maximum amplitude of $\delta c^2/c^2 = 15\%$. The travel-time map corresponding to the distance $\Delta = 30.55$ Mm is shown in the left panel of Figure 6. In the right panel, the quiet travel-time map has been subtracted: the noise level is considerably reduced, as mentioned in § 3. The travel-time map in the left panel looks very similar to maps computed for datacubes obtained from the Michelson Doppler Imager (MDI) instrument on board the *Solar and Heliospheric Observatory (SOHO)* spacecraft, and because the noise levels between the artificial and real data are comparable, the choice of the excitation mechanism is somewhat justified. Figure 7 further shows the impact of the noise subtraction method on the travel-time maps.

In Figure 8, the dependence of the azimuthally averaged mean travel-time perturbations, $\delta\tau_{mean}(\mathbf{r}, \Delta)$, on the radial distance from the center of the perturbation is shown by the thick solid line. The rms variation σ of $\delta\tau_{mean}(\mathbf{r}, \Delta)$ is an estimate of the uncertainty on this value (the error bars in Fig. 8 are $\pm\sigma$). The thin solid line represents the average of the difference travel-time perturbation $\delta\tau_{diff}(\mathbf{r}, \Delta)$ and is close to zero, as expected from the absence of flows in our simulation.
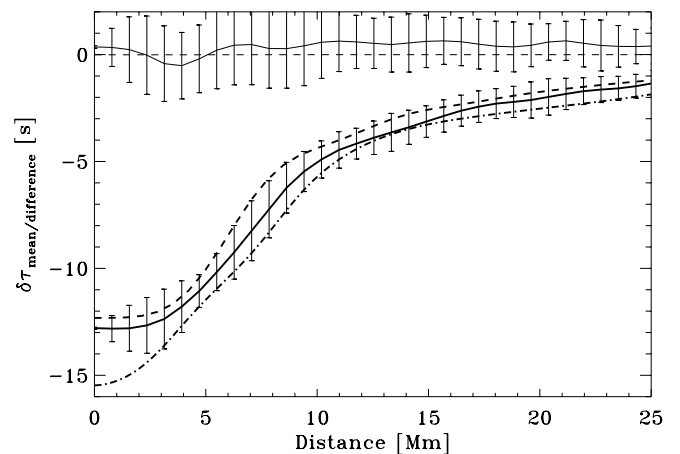

Fig. 7.—Cut across the mean travel-time perturbation map $\delta\tau_{mean}(\mathbf{r}, \Delta)$ from Fig. 6 at $y = 50$ Mm. The thin line is from before the quiet map subtraction, and the thick line is from after the subtraction.

Fig. 8.—Azimuthal average of $\delta\tau_{mean}(\mathbf{r}, \Delta)$ (*thick solid line*) and $\delta\tau_{diff}(\mathbf{r}, \Delta)$ (*thin solid line*) for $\Delta = 30.55$ Mm, as a function of the radial distance to the sound-speed perturbation center (simulation). The dot-dashed line shows the mean travel-time shift computed with ray kernels for the background model in the simulation. The dashed lines show the solution to the forward problem using Born sensitivity kernels. The solar model in the simulation is slightly different from the model used to compute the Born kernels, contributing to the difference between the two travel-time curves.

4.2. *Validation*

A first test of the effectiveness of the numerical algorithm is to see if the simulated power spectrum looks reasonable in comparison to the solar modal spectrum. The spectrum shown in Figure 5a seems to satisfy this basic criterion. Secondly, through ray calculations, we can estimate the mean travel times associated with the background solar model. Although we do not show this here, comparisons between the ray-predicted travel times and those obtained from the quiet simulations further fortify our confidence in the computational method. Next, using Born sensitivity kernels for sound-speed perturbations (Birch et al. 2004), we can derive the expected $\delta\tau_{\mathrm{mean}}(\boldsymbol{r}, \Delta)$ (or $\delta\tau_{\mathrm{diff}}$) by evaluating the right-hand side of the following equation (forward problem):

$$\delta\tau_{\mathrm{mean/diff}}(\boldsymbol{r}, \Delta) =$$
$$\int\!\!\int_S d\boldsymbol{r}' \int_{-d}^{0} dz\, K_{\mathrm{mean/diff}}(\boldsymbol{r} - \boldsymbol{r}', z; \Delta)\frac{\delta c^2}{c^2}(\boldsymbol{r}', z), \quad (7)$$

where S is the area of the Doppler velocity datacube, d is its depth, $K_{\mathrm{mean/diff}}(\boldsymbol{r} - \boldsymbol{r}', z; \Delta)$ are the sensitivity kernels for distance Δ, and $\delta\tau(\boldsymbol{r}; \Delta)$ is defined as the travel-time shift at the center of the annulus (whose radius is Δ). The kernels we use to calculate the right-hand side of equation (7) were computed for the standard solar model S (Christensen-Dalsgaard et al. 1996), implying that the comparison is mostly qualitative, since we use a slightly altered description of the near-surface layers (Hanasoge et al. 2006). These are point-to-point kernels, azimuthally averaged the same way as the cross-covariances to produce point-to-annulus kernels. The ingoing and outgoing point-to-annulus kernels are then either averaged or subtracted in relation to $\delta\tau_{\mathrm{mean}}$ and $\delta\tau_{\mathrm{diff}}$.

In Figure 8, the dashed line shows the azimuthal average of $\delta\tau_{\mathrm{mean}}(\boldsymbol{r}, \Delta)$ obtained from equation (7), while the solid line shows an azimuthal average of the mean travel times obtained from the simulation. As expected, the two lines are not quite identical; this is perhaps due to small differences between phase-speed filter parameters and the background models in the two cases. Two independent methods were used in this comparison: the Born approximation, to solve the forward problem, and the wavefield simulation in conjunction with a code to extract travel times from these calculations. Next we check to see if the mean travel-time shifts computed with the ray approximation, shown by the dot-dashed line in Figure 8, are comparable. As expected, ray theory, which does not account for wave front healing (e.g., Hung et al. 2001), overestimates these shifts but is still relatively accurate. It is gratifying to see that although the approaches in these methods differ greatly, there is still close agreement between the travel times. At this juncture, we consider the numerical method validated for the cases discussed here.

5. KERNELS

Extending equation (7) to account for arbitrary perturbations, $\delta q(\boldsymbol{r}')$, we have

$$\delta\tau_{\mathrm{mean/diff}}(\boldsymbol{r}; \Delta) =$$
$$\int\!\!\int_S d\boldsymbol{r}' \int_{-d}^{0} dz\, K_{\mathrm{mean/diff}}(\boldsymbol{r} - \boldsymbol{r}', z; \Delta)\delta q(\boldsymbol{r}', z), \quad (8)$$

where for future discussions, we adopt the notation of Duvall et al. (2006); namely, that $\delta\tau(\boldsymbol{r}; \Delta)$ is defined as the travel-time shift at position $\boldsymbol{r}$, located at the center of two observation points
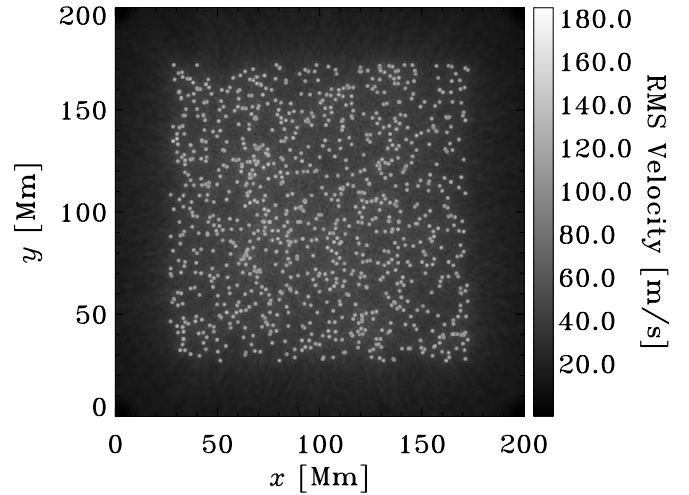

Fig. 9.—Time-averaged rms of the difference in velocities from a simulation with 1000 randomly located 1 Mm sized source suppressions and its unperturbed counterpart. In the vicinity of a source suppression, acoustic velocities are altered; therefore, the hundreds of local maxima in this difference map show where the sources are diminished. The perturbations are approximately limited to a 150×150 Mm^2 interior square, allowing travel-time shifts associated with all the anomalies to be computed.

spaced a distance Δ apart. With this change in definition of travel times, we move from the center-to-annulus geometry of the previous section (§ 4) to a point-to-point description. There are numerous kinds of anomalies (changes in density, sound speed, pressure, source amplitude, and magnetic fields, to name a few), each of which is associated with a specific kernel. For perturbations that are spatial delta functions with magnitude M, of the form $\delta q(\boldsymbol{r}', z) = M\delta(\boldsymbol{r}')\delta(z - z_0)$, it may be verified from equation (8) that the convolution on the right-hand side reduces to $(2\pi)^3 MK(\boldsymbol{r}, z_0; \Delta)$ (the 2π factors are dependent on the definition of the delta function), the conclusion being that the travel-time shifts and the kernel are identical to within a proportionality constant in this limit. Duvall et al. (2006) incorporated this approximation to derive a kernel from observations of thousands of thin magnetic elements on the Sun, justifying it through the argument that the magnetic flux tubes were all much smaller than the wavelength of the f-modes used in the analysis. We apply the same technique to derive (1) a sound-speed sensitivity kernel (for p-modes) and (2) a source amplitude kernel (using the f-mode as the diagnostic agent) from 1000 randomly placed small (1 Mm in size) source suppressions (see Fig. 9) for the solar model and setup in our computations.

We choose this set of kernels to study because Gizon & Birch (2002) and Birch et al. (2004) have constructed f-mode source disturbance and p-mode sound-speed perturbation kernels, respectively, allowing us the luxury of comparison. In the source perturbation kernel of Gizon & Birch (2002), elliptical features are absent and only hyperbolic features associated with multiple sources are seen; the sound-speed kernels of Birch et al. (2004) contain a mixture of both elliptical and hyperbolic ridges. The ability to recover a source kernel from the simulation of Figure 9 is important because we demonstrate proof of concept of the kernel measurement method devised by Duvall et al. (2006). The balance between the randomness of the locations of these elements and the determinism of the sense of the perturbation (all sources are reduced) seems to result in an average structure in the travel times that looks remarkably like the source perturbation kernel from Gizon & Birch (2002), as seen in panels *a*–*d* of Figure 10.
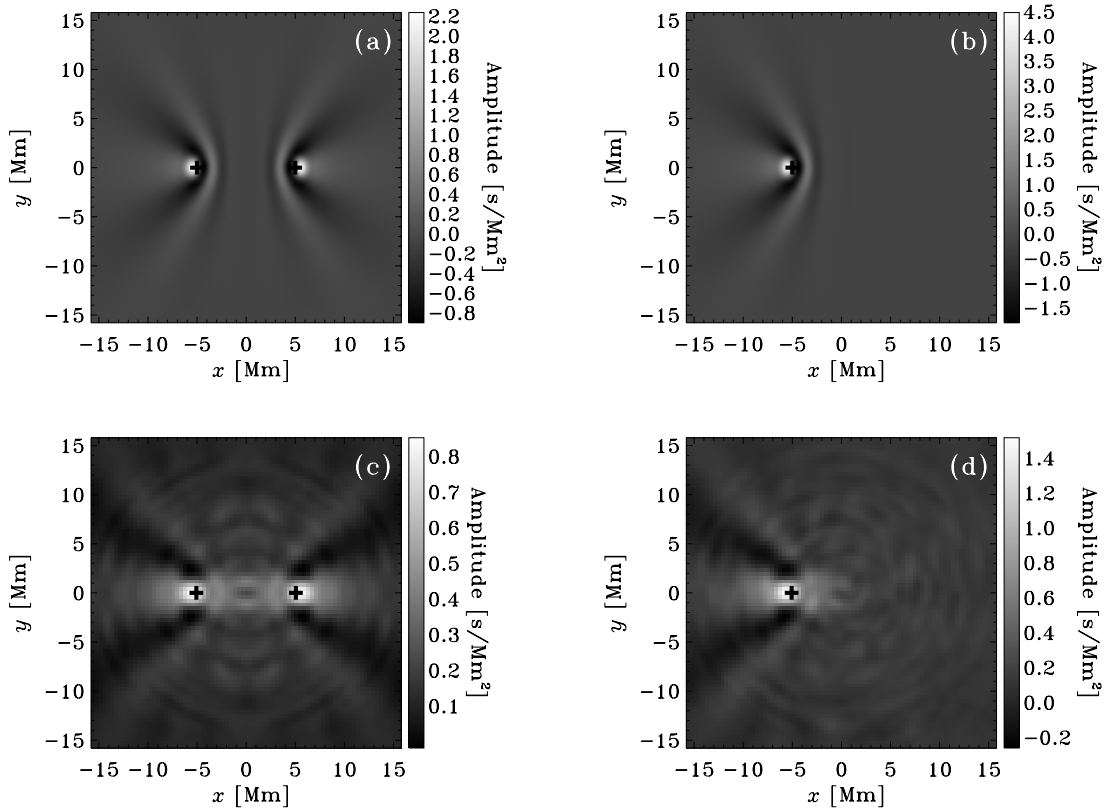
FIG. 10.—Kernels of the *f*-mode source perturbations. Panels (*a*) and (*b*) show the mean and left-to-right one-way kernels from Gizon & Birch (2002), respectively. Plus signs show the measurement points. Upon systematically derotating and averaging the travel-time shifts associated with the 1000 locally deactivated sources from Fig. 9, subtracting the noise, and scaling the travel times as described in Appendix B, the kernels in panels (*c*) and (*d*) emerge. The lack of elliptical features in these kernels is perhaps explained by the independence of the sources from the wavefield, both in the theory of Gizon & Birch (2002) and in the simulations. Panel (*d*) is especially compelling because, according to theory, left-to-right one-way travel times should only be shifted for those points that lie closer to the left measurement point. The power profile of the *f*-ridge used to recover the travel-time shifts is shown in Fig. 1.

The technique through which the SNR of the data is improved by enough that it becomes possible to see the travel times associated with these small features is described in detail by Duvall et al. (2006). First, the data are phase-speed filtered to either restrict the acoustic spectrum to waves that travel a given distance, Δ, between bounces or to isolate the *f*-mode ridge. For all points $\boldsymbol{r} = (x, y)$ in the domain of interest (eq. [8]), the temporal cross-correlation is obtained by inverse Fourier transforming $\tilde{C}$, where

$$\tilde{C}(\omega, x + \delta x/2, y + \delta y/2) = \tilde{v}^*(\omega, x, y)\tilde{v}(\omega, x + \delta x, y + \delta y),$$

(9)

which is subsequently fitted to obtain travel times. In equation (9), ω is the frequency, $v(t, x, y)$ is the velocity signal at time t and spatial location (x, y), $\tilde{v}(\omega, x, y)$ represents the Fourier transform of $v(t, x, y)$, $\tilde{v}^*$ is the complex conjugate of $\tilde{v}$, and arctan $(\delta y/\delta x)$ is the orientation of the travel-time map. Within the limits of spatial resolution, there were 77 possible orientations for the simulation that contained the sound-speed perturbation [120×120 Mm^2 in the (x, y)-plane, resolved with 144^2 points] and 83 orientations for the source perturbation case [200×200 Mm^2 in the (x, y)-plane, resolved with 512^2 points]. Subsequently, the resulting two-point travel times were derotated by an angle of arctan $(\delta y/\delta x)$ and averaged. For the simulation with 1000 suppressions, the image is not only derotated but averaged around each feature, corresponding to a net total of 83,000 averages. The SNR is still not high enough with this

degree of averaging; only after the travel times of the quiet datacube, obtained through the same averaging process, are subtracted do the hyperbolae of the kernel become clearly visible. A similar averaging algorithm is used to produce the sound-speed kernel (see Fig. 12 below), albeit the wavefield was simulated in the presence of only one anomaly.

5.1. Source Kernels

Although the magnitudes and the hyperbolic features are somewhat different, kernels obtained from simulations and theory (Fig. 10) possess a strong resemblance. It is seen from Figure 1 that the *f*-mode power distribution is able to match the observations (and the excitation model of Gizon & Birch 2002) quite well, so frequency effects are not significant contributors to the differences in the hyperbolic structures. One possible explanation could be the damping, which is included in theory but not in the simulations. The absence of solar-like damping has two important effects: (1) mode power distribution and line widths differ from the solar counterparts and (2) waves are correlated across larger distances. The latter implies that travel-time shifts of waves remain coherent over longer length scales than in the Sun or the model of, e.g., Gizon & Birch (2002). The other issue concerns the differing magnitudes of the kernels; perhaps the method described in Appendix B to scale the travel times is only approximate. Moreover, the theoretical kernel of Gizon & Birch (2002) has a spatial integral of zero, while the kernel obtained from the simulation has a positive bias of 0.5 s (calculated as the mean travel-time shift of a small off-center region).
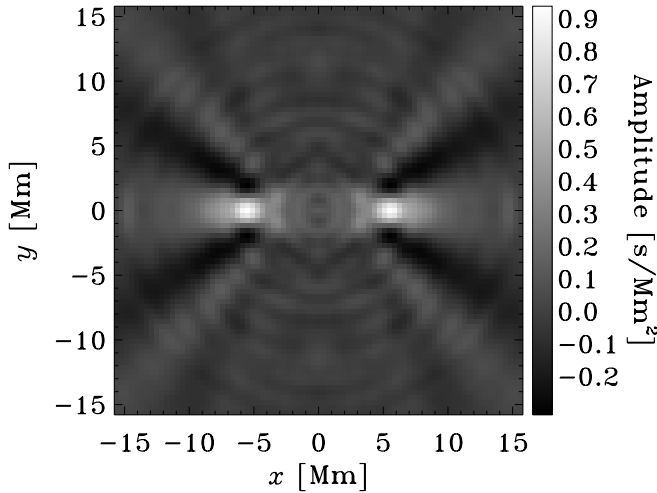
FIG. 11.—Source kernel obtained by suppressing approximately half the sources and doubling the strengths of the rest. The integral of the kernel is an order of magnitude smaller than the amplitude of the kernel.

The travel-time shifts observed in this case are due to reductions in the cross-correlation amplitude because of local depressions in source strengths. The cross-correlations are biased in the sense of decreased amplitude because all the sources have been suppressed, possibly leading to a nonzero value of the integral of the kernel. In an attempt to correct for this, we tried another case in which approximately half the perturbed sources were suppressed and the other half were amplified. To obtain a meaningful average kernel (shown in Fig. 11), the sign of the travel times for the source suppressions was flipped, while the source amplification counterparts were left untouched. In this case, the integral of the kernel is much smaller than the amplitude, indicating that the bias in the kernel of Figure 10*c* is most probably caused by the systematic sense in the perturbation (suppression).

5.2. *Sound-Speed Kernels*

The sound-speed kernel of Figure 12*a* was derived for the same measurement distance (12.4 Mm) as the one in Figure 12*b* (reproduced from the bottom right panel of Fig. 10 from Birch et al. 2004). Although there are many differences in the approaches, not the least being the background model and damping rates, the agreement is excellent. This result also illustrates the

ability of the method of noise subtraction to remove the noise without affecting the signal itself. Although not shown here, we have noted that as the central frequency of the wavepacket used to construct the kernel increases, the ellipses become even more "elliptical," an indicator of raylike behavior. In general, there is a definite dependence of the shape of the kernel on the filter parameters.

6. CONCLUSIONS

A numerical method to compute the 3D wavefield in a solar-like medium was discussed and implemented. The concept of noise subtraction, a technique whereby the realization noise can be significantly reduced, was introduced. This method is quite useful in reducing computational cost by making it possible to achieve large SNRs even with short simulations. Results from the simulations were validated using comparisons between the travel times obtained (1) from the surface focusing method of time-distance helioseismology, (2) through the application of approximate Born sensitivity kernels, and (3) from ray theory. The results agree rather well, showing the validity of these independent approaches for this particular situation.

We ran a simulation with 1000 randomly located suppressed sources that was subsequently analyzed by the feature method of Duvall et al. (2006) to obtain travel-time shifts associated with the average diminished source. The result closely resembles the source perturbation kernel of Gizon & Birch (2002). A sound-speed kernel for parameters similar to a case considered by Birch et al. (2004) was derived. The agreement between Born theory and simulations in conjunction with time-distance helioseismology is impressive. It lends greater confidence to the technique of direct measurements of kernels from data (Duvall et al. 2006) and the method of noise subtraction. It is interesting to note that the structure of the kernels is quite sensitive to the relevant frequency bandpass; high-frequency wave kernels have pronounced elliptic features displaying raylike behavior. The source and sound-speed kernels shown here contain aspects of multiple scattering and in general are not bound by the assumptions of the Born approximation. We can also derive sensitivity kernels for various types of perturbations such as anomalies in density, pressure, Γ_1, etc., that are relatively difficult to compute in the Born limit.

The price we currently pay for the ability to perform these simulations is reduced realism. Damping, which is not accounted for in our computations, is an important contributor, affecting travel times (e.g., Woodard 1997) and in general changing the
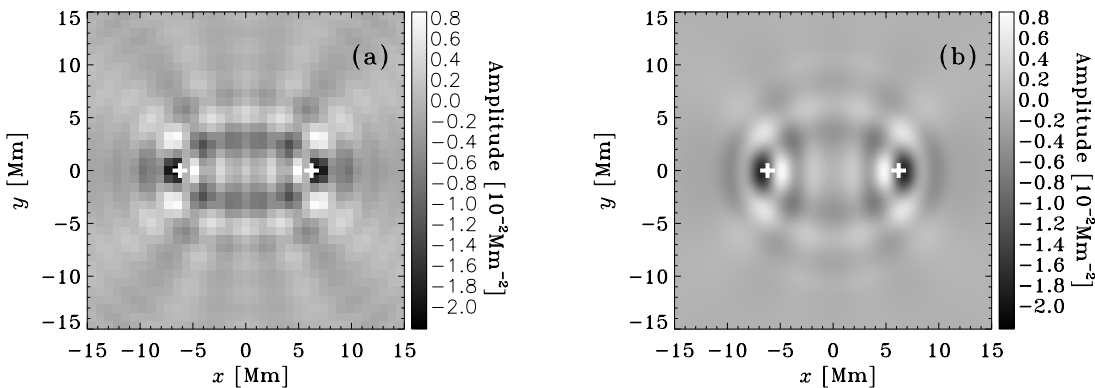

FIG. 12.—(*a*) Sound-speed kernel from 24 hr of simulated data (12 perturbed + 12 quiet). (*b*) Sound-speed kernel reproduced from the bottom right panel of Fig. 10 of Birch et al. (2004). The plus signs mark the measurement points. The kernels have been multiplied by the sound speed at the photospheric level in both cases; units are in 10^{-2} Mm^{-2}. The agreement is striking. The circular features in (*a*) are generated by the repeated derotation of travel-time shifts and hence are mainly noise. Both hyperbolic and elliptical features are visible in this kernel. The power profile of the modes utilized to construct the kernel in (*a*) is shown in Fig. 1*b*.

distribution of modal power and the line widths. A further approximation in our simulations is the use of an altered background state; the standard solar model S makes it difficult to perform linear simulations due to the inherent convective instability of the near-surface layers. It is important for sophisticated forward models to be able to incorporate damping and an accurate solar model.

The effects of diffractive or wave front healing, a hotly contested phenomenon in geophysics, are currently being investigated in the context of helioseismology through these simulations. We will be able to place bounds on detectability and the accuracy of inversions and to study vector effects such as flows. It will also be very exciting to disentangle magnetic field effects and determine

if we have a reasonable understanding of the interior structure of sunspots.

APPENDIX A

PHASE SPEEDS

Eleven filters of mean phase speed v and width δv are used for different ranges of annulus radii Δ, as shown in Table 1. The first column gives the annulus index, and the last column gives the center time t_0 of the window function used to measure first-bounce travel times (see § 4).

APPENDIX B

SCALING KERNELS

Since it is numerically impossible to capture a delta function, we define the anomalies by the following sharply decaying functions:

$$\frac{\delta c^2}{c^2} = 0.1\left\{1 - \frac{1}{1 + \exp\left[8.2(1 - r)\right]}\right\}, \tag{B1}$$

$$\frac{\delta a}{a} = -\left\{1 - \frac{1}{1 + \exp\left[8.9(1 - \tilde{r})\right]}\right\}, \tag{B2}$$

where $r = (x^2 + y^2 + z^2)^{1/2}$ is in units of Mm and $(0, 0, 0)$ is the center of the perturbation (it is vertically localized at the level of the photosphere). We use the notation of Gizon & Birch (2002) to describe a source perturbation in equation (B2), where a is the strength of the unperturbed source and the deactivated source is located around the point (x_0, y_0, z_0), with $\tilde{r} = [(x - x_0)^2 + (y - y_0)^2]^{1/2}$ (also in units of Mm) and $z_0 = -200$ km. Since the f-mode is the diagnostic agent in this case, we assume that the anomaly is essentially two-dimensional (2D) in nature. To transform travel-time shifts to kernel magnitudes for the sound-speed perturbation case, consider the function from equation (B1) applied to equation (7). Assuming that the kernel varies much slower than the perturbation, we can rewrite equation (7) as

$$\delta\tau_{\mathrm{mean/diff}}(\boldsymbol{r}) = K_{\mathrm{mean/diff}}(\boldsymbol{r}, 0; \Delta) \int \int \int_{\odot} \frac{\delta c^2}{c^2}(\boldsymbol{r}', z)\, d\boldsymbol{r}'\, dz, \tag{B3}$$

TABLE 1
ANNULI AND PHASE-SPEED FILTER PARAMETERS

Index	Mean Δ (Mm)	Δ (Mm)	v (km s^{-1})	δv (km s^{-1})	t_0 (minutes)
1	6.20	03.7, 04.95, 06.20, 07.45, 08.7	16.40	2.63	19.00
2	8.70	06.2, 07.45, 08.70, 09.95, 11.2	19.28	2.63	19.17
3	11.60	08.7, 10.15, 11.60, 13.05, 14.5	22.26	2.63	20.00
4	16.95	14.5, 15.72, 16.95, 18.17, 19.4	27.24	3.68	25.00
5	24.35	19.4, 21.87, 24.35, 26.82, 29.3	35.73	3.94	27.50
6	30.55	26.0, 28.27, 30.55, 32.82, 35.1	40.06	3.94	29.17
7	36.75	31.8, 34.27, 36.75, 39.22, 41.7	43.25	3.94	30.83
8	42.95	38.4, 40.67, 42.95, 45.22, 47.5	49.20	3.94	33.33
9	49.15	44.2, 46.67, 49.15, 51.62, 54.1	55.80	4.46	35.00
10	55.35	50.8, 53.07, 55.35, 57.62, 59.9	59.25	4.46	36.67
11	61.65	56.6, 59.12, 61.65, 64.18, 66.7	64.37	4.46	38.33

which when integrated merely becomes the finite volume of the perturbation in equation (B1). A similar 2D area integration ($z = -200$ km) is carried out for the source perturbation. Calculating these integrals, the kernel for the sound-speed perturbation (in units of s Mm^{-3}) is

$$K_{\mathrm{mean/diff}}(\boldsymbol{r},\,0;\Delta) = 4.164\delta\tau_{\mathrm{mean/diff}}(\boldsymbol{r}), \tag{B4}$$

and for the *f*-mode source kernel (in units of s Mm^{-2}),

$$K_{\mathrm{mean/diff}}(\boldsymbol{r},\,0;\Delta) = -0.3056\delta\tau_{\mathrm{mean/diff}}(\boldsymbol{r}). \tag{B5}$$

REFERENCES

Birch, A. C., & Kosovichev, A. G. 2000, Sol. Phys., 192, 193
Birch, A. C., Kosovichev, A. G., & Duvall, T. L., Jr. 2004, ApJ, 608, 580
Braun, D. C., Duvall, T. L., Jr., & Labonte, B. J. 1987, ApJ, 319, L27
Christensen-Dalsgaard, J., et al. 1996, Science, 272, 1286
Couvidat, S., Birch, A. C., & Kosovichev, A. G. 2006, ApJ, 640, 516
Couvidat, S., Birch, A. C., Kosovichev, A. G., & Zhao, J. 2004, ApJ, 607, 554
Duvall, T. L., Jr., Birch, A. C., & Gizon, L. 2006, ApJ, 646, 553
Duvall, T. L., Jr., Jefferies, S. M., Harvey, J. W., & Pomerantz, M. A. 1993, Nature, 362, 430
Duvall, T. L., Jr., et al. 1997, Sol. Phys., 170, 63
Gizon, L., & Birch, A. C. 2002, ApJ, 571, 966
———. 2005, Living Rev. Sol. Phys., 2, 6
Hanasoge, S. M., & Duvall, T. L., Jr. 2006, in Proc. *SOHO* 18/GONG 2006/ HELAS I: Beyond the Spherical Sun, ed. K. Fletcher (ESA SP-624; Noordwijk: ESA), 40.1
———. 2007, Astron. Nachr., 328, 319
Hanasoge, S. M., et al. 2006, ApJ, 648, 1268
Hill, F. 1988, ApJ, 333, 996
Hu, F. Q., Hussaini, M. Y., & Manthey, J. L. 1996, J. Comput. Phys., 124, 177
Hung, S.-H., Dahlen, F. A., & Nolet, G. 2001, Geophys. J. Int., 146, 289

Jensen, J. M., Olsen, K. B., Duvall, T. L., & Jacobsen, B. H. 2003, in Proc. *SOHO* 12/GONG+ 12 2002: Local and Global Helioseismology, ed. H. Sawaya-Lacoste (ESA SP-517; Noordwijk: ESA), 319
Jensen, J. M., & Pijpers, F. P. 2003, A&A, 412, 257
Kosovichev, A. G., & Duvall, T. L., Jr. 1997, in SCORe '96: Solar Convection and Oscillations and their Relationship, ed. F. P. Pijpers, J. Christensen-Dalsgaard, & C. S. Rosenthal (Dordrecht: Kluwer), 241
Lele, S. K. 1992, J. Comput. Phys., 103, 16
Orszag, S. A. 1970, J. Fluid Mech., 41, 363
Parchevsky, K., & Kosovichev, A. G. 2006, in Proc. *SOHO* 18/GONG 2006/ HELAS I: Beyond the Spherical Sun, ed. K. Fletcher (ESA SP-624; Noordwijk: ESA), 39.1
Shelyag, S., Erdélyi, R., & Thompson, M. J. 2006, ApJ, 651, 576
Thompson, K. W. 1990, J. Comput. Phys., 89, 439
Tong, C. H., Thompson, M. J., Warner, M. R., Rajaguru, S. P., & Pain, C. C. 2003, ApJ, 582, L121
Werne, J., Birch, A., & Julien, K. 2004, in Proc. *SOHO* 14/GONG 2004, Helio-and Asteroseismology: Towards a Golden Future, ed. D. Danesy (ESA SP-559; Noordwijk: ESA), 172
Woodard, M. F. 1997, ApJ, 485, 890